Prostate Cancer Diagnosis Based on the Segmentation and Analysis of NIR Images Obtained Using Two PSMA-1 Based PDT Conjugates PSMA-1-Pc413 and PSMA-1-IR700

Rachid Sammouda[*]

Department of Computer Sciences, King Saud University, Riyadh, KSA

Email: rsammouda@ksu.edu.sa

Abstract

Prostate cancer is among the widespread men's diseases in the world. Prostatectomy has been the strength treatment for men with restricted prostate tumor. On the other hand, surgery, frequently can cause some side effects initiated from damage and removal of nerves and muscles surrounding the prostate. Prostate-specific membrane antigen (PSMA), a type II membrane antigen highly expressed in prostate cancer, has been an attractive target for imaging and therapy. Photodynamic therapy (PDT) is a non-invasive therapy which is used clinically in the treatment of various cancers and other diseases. The objective of this study is to segment and analyze the near-infrared (NIR) images of prostate cancer cells obtained using developed low molecular weight PSMA-targeting PDT agents, which would provide image-guidance for prostate tumor resection and allow for subsequent PDT to eliminate un-resectable or remaining cancer cells. The segmentation of NIR color images, of prostate cancer cells, is performed using Unsupervised Hopfield Neural Network Classifier (UHNNC) which gives better distribution of pixels among a predefined number of clusters. The clusters' statistics needed for analysis are given using ENVI software product for image analysis.

----

* Corresponding author.

The results of this study show that the combination of the segmentation results with the clusters' statistics with the appropriate PSMA, creates a better visualization of the cancerous tissues and help medical doctors for a more accurate diagnosis and surgery planning.

Keywords: Prostate cancer; near-infrared (NIR) images; molecular weight PSMA-targeting PDT agents.

1. Introduction

(As the introduction of Prostate-specific membrane antigen (PSMA) analysis, significantly additional males have been diagnosed and treated for prostate cancer [1]. Approximately 220,800 new diagnoses and 27,540 deaths from the disease are projected in 2015 among men in the United States [2]. Over 90% of men have localized tumors at initial screenings and are candidates for radical prostatectomies [3]. However, at surgery, cancer has been shown to extend outside the prostate (pathological stage C) in 20-42% of patients [4] and surgery fails to halt the disease in approximately 20% of the patients who undergo radical prostatectomy, and over a 60% recurrence rate of this disease in this population has been reported [5-7].

Although surgeons are experienced with this disease, radical prostatectomy remains an imperfect intervention. During surgery, it's difficult for surgeons to access the invasion of prostate cancer; therefore, many malignant nodules escape detection, leading to disease recurrence. A retrospective multivariate analysis by Wright *et al.* of incomplete resection of prostate cancer in over 65,000 patients who underwent radical prostatectomies [8] found that positive surgical margins were associated with a 2.6-fold increased unadjusted risk of prostate cancer specific mortality and are an independent predictor of mortality.

This study also underlined the need for surgeons to optimize surgical techniques to achieve the negative surgical margins essential for sound oncological outcomes. Surgical achievement of this without side effects is a challenge, however, because the prostate is surrounded by many nerves and muscle fibers controlling different excretory and erectile functions that are difficult but necessary to avoid. In 1983 Walsh defined nerve locations around the prostate and inspired a number of "nerve-sparing" surgical approaches, including robotic-assisted laparoscopic prostatectomy [9]. Unfortunately, the success of these approaches to mitigate side effects is mixed [10, 11] and surgical approaches to prostate cancer are still associated with significant morbidity, e.g. incontinence (3-74%) and impotence (30-90%) [12-17]. There remains an unmet clinical need to improve surgical techniques for identifying and removing cancerous tissue without damaging surrounding tissues during prostatectomy. Recently, Neuman *et al.* have shown that near-infrared (NIR) fluorescence probe YC-27 can improve the surgical treatment of prostate cancer and reduce the rate of positive surgical margins in real-time laparoscopic extirpative surgery [18].

Photodynamic Therapy (PDT) is a non-invasive therapy, which is used clinically in the treatment of cancers and other diseases [19-21]. PDT uses photosensitizers which are pharmacologically inactive until they are exposed to light in the presence of oxygen. The active drug forms reactive oxygen species such as singlet oxygen to kill nearby cells. Various agents, including porphyrins and phthalocyanines have been examined as photosensitizers [22-24]. Most photosensitizers are fluorescent and emit near-infrared (NIR) light that can be used for *in vivo*

imaging to identify the location of cancer cells and provide image-guided PDT treatment potentially leading to improved therapeutic accuracy and outcome [22]. The main challenge for PDT treatment is off-target tissue accumulation and activation of photosensitizer leading to cell death in normal tissue [25]. Development of a highly selective delivery method for photosensitizers to minimize side effects and generate better therapeutic outcomes would be optimal.

PSMA is a unique membrane bound glycoprotein originally discovered in the androgen-dependent LNCaP human prostate adenocarcinoma cell line using a monoclonal, mAb 7E11C-5.3 [26]. PSMA is overexpressed on prostate cancer. Expression of PSMA in cancer tissues correlates with the stage of disease and Gleason score [27]. PSMA expression is also higher in prostate cancer cells from hormone-refractory patients [27, 28] and increased PSMA expression has been shown to be an independent marker of disease recurrence [28-30]. In addition to being overexpressed in prostate cancer, PSMA is also expressed in the neovasculature of many solid tumors [31]. PSMA has served as a promising target for both imaging [32-34] and treatment of prostate cancer [35-37]. A peptide-based, highly negatively charged PSMA ligand (PSMA-1) was developed and used for PSMA-targeted imaging of prostate cancer [38, 39].

In this study, we present the segmentation and analysis results the NIR prostate images obtained using two PSMA-1 based PDT conjugates, PSMA-1-Pc413 Figure1.A and PSMA-1-IR700 Figure1.B. Pc413 is an analogue of second generation phthalocyanine PDT drug Pc4 which is currently in clinical trials [40], and IR700 is a commercially available near-infrared dye which has been shown to have PDT activities [41-43].
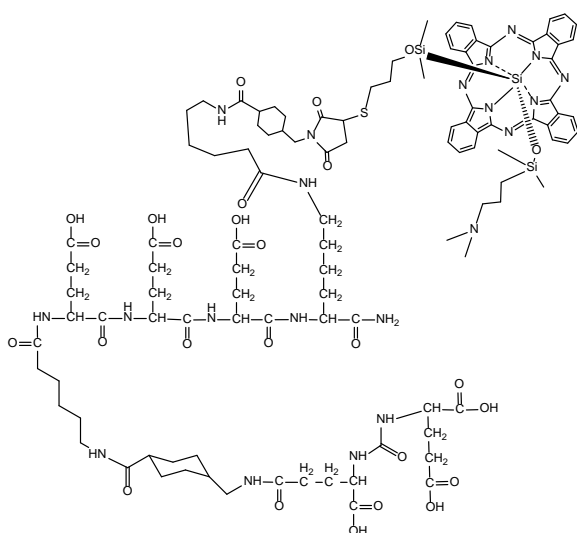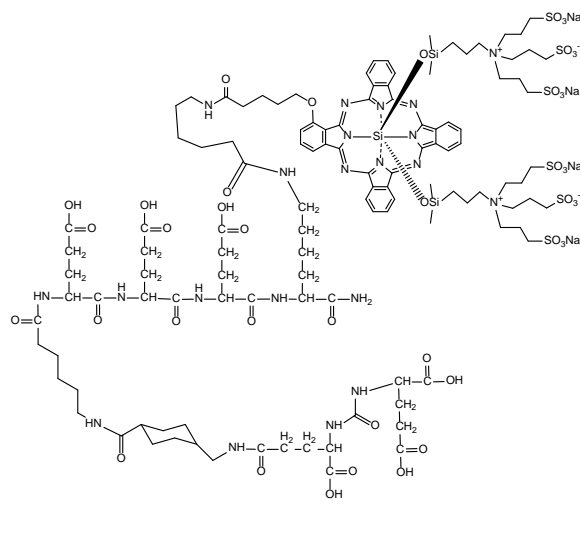

Figure1.A. Structure of PSMA-1-Pc413   Figure1.B. Structure of PSMA-1-IR700

Figure 1: Structures of PSMA-1-Pc413 Figure1.A and PSMA-1-IR700 Figure1.B.

2. Methods and Materials

PSMA targeting peptide PSMA-1 was synthesized by Fmoc chemistry as previously reported [39]. All the other

chemicals were purchased from Sigma-Aldrich Inc., St. Louis, MO, USA. High Performance Liquid Chromatography (HPLC) was performed on a Shimadzu HPLC system equipped with a SPD-20A prominence UV/visible detector and monitored at a wavelength at 220 nm for PSMA-1-SMCC or 350 nm for PSMA-1-Pc413 and PSMA-1-IR700.

For *in vivo* NIR imaging studies, animal experiments were performed according to policies and guidelines of the animal care and use committee at Case Western Reserve University (IACUC#120024). Six to eight weeks old male athymic nude mice were implanted subcutaneously with 1×10^6 of PSMA-negative PC3flu and PSMA-positive PC3pip on the left and right dorsum respectively. Animals were ready to use when tumors reached the size at about 10 mm. PSMA-1-PDT was injected intravenously via the tail vein. Fluorescence imaging was performed using the Maestro *in Vivo* Imaging system (Perkin-Elmer, Waltham, MA). During imaging, mice were anaesthetized with isoflurane. After imaging, the mice were euthanized and tissues were harvested for *ex vivo* imaging. For *in vivo* competition experiments, mice were co-injected with 1 nmol of PSMA-1-Pc413 and 1000 nmol of ZJ-MCC-Ahx-YYYG, an analogue of PSMA-1 with similar binding affinity [38], or 1 nmol of PSMA-1-IR700 probes and 1000 nmol of PSMA-1. Different competitors were used for PSMA-1-Pc413 and PSMA-1-IR700 due to their different pharmacokinetic behaviors. Multispectral images were unmixed into their component spectra (PSMA probes, autofluorescence, and background) and these component images were used to quantitate the average fluorescence intensity associated with the tumors by creating regions of interest (ROIs) around the tumors. The two probes reported in [44] were found to be effective as theranostic probes allowing both targeted-bioimaging and targeted-photodynamic therapy of prostate cancer. The tumors were extracted 24 hours post the PDT treatment and processed by hematoxylin and eosin staining. Pathological analysis showed that the nuclei in cancer cells treated with PSMA-1-PDT probes were much smaller compared to untreated tumors, indicating that the cells were damaged as shown in Figure 2.

Hopfield Neural Network Segmentation Technique: Segmentation shows a critical role in therapeutic and biomechanical fields, such as assisting radiologists and medical doctors to improve their diagnosis. In the past few decades, researchers have proposed many effective algorithms to perform the computer aided segmentation. The successful implementation of modern mathematical and physical techniques, such as Bayesian's analysis, template matching and deformable models, greatly enhances the accuracy of segmentation results. Compared with common image segmentation algorithms, the ones used for medical images need more concrete backgrounds and must satisfy the complex practical requirements. A good survey about these techniques are discussed in [45]. In our previous work, we have UHNNC to segment different type of medical and natural color images [46, 47], the segmentation results have been appreciated with respect to the multi-dimensionality of the data type used for segmentation. This means that UHNNC gives better segmentation results as far as getting more information about the pixel of the scene under segmentation. Here, we adapt the UHNNC to segment the NIR color image, samples are shown in Figure 2, and we analyze the clusters of the segmentation results with respect to the case available medical information and tissues features. UHNNC architecture consists of a grid of NM neurons with each column representing a class and each row representing a pixel, N represents the size of the given image and M represents the number of clusters, the latter is given as a priori information. The network is designed to classify the feature space without teacher based on the compactness of each class calculated using a distance measure.
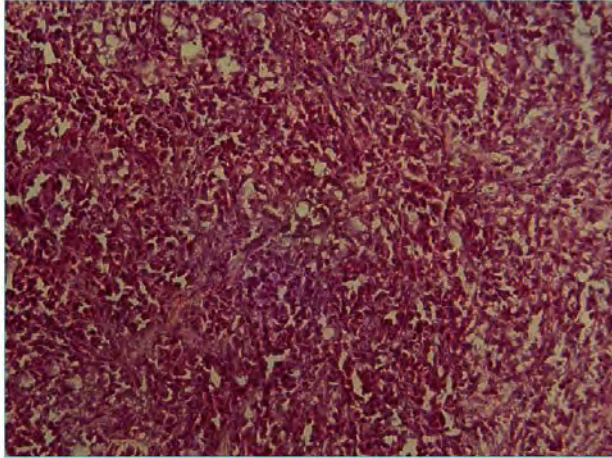
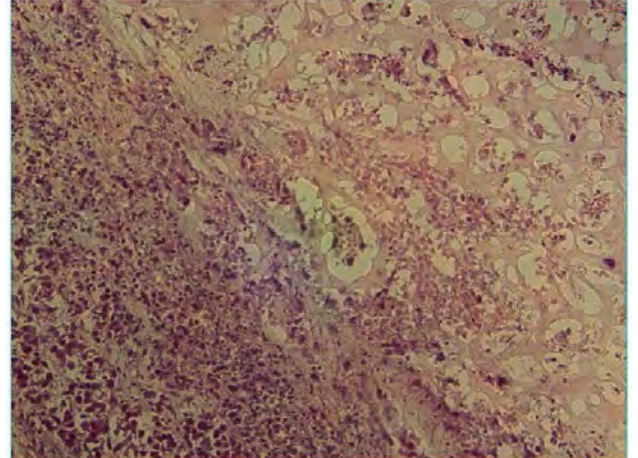Figure 2. (A) PC3pip tumor; (0.5 mg/kg PSMA-1-Pc413); (no light irradiation)

Figure 2. (B) PC3pip tumor; (0.5 mg/kg PSMA-1-Pc413); with (150J/cm2 light irradiation)
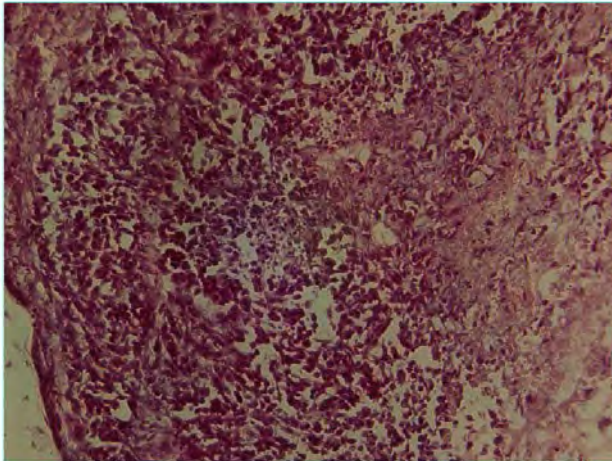
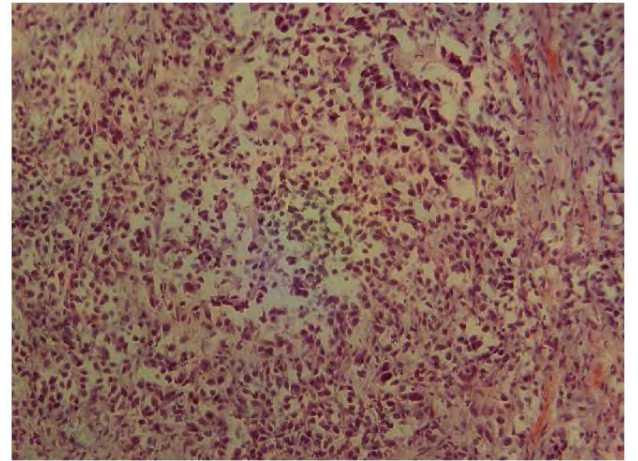Figure 2. (C) PC3pip tumor; (0.5 mg/kg PSMA-1-IR700); (no light irradiation)

Figure 2. (D) PC3pip tumor; (0.5 mg/kg PSMA-1-IR700); with (50J/cm2 light irradiation)

Figure 2: Images of the PC3pip tumors receiving PSMA-1-PC413 and PSMA-1-IR700 wit and without light irradiation.

The segmentation problem is formulated as a partition of N pixels of P features among M clusters or regions, such that the assignment of the pixels minimizes the cost-term of the energy (error) function:

$$E = \frac{1}{2}\sum_{k=1}^{N}\sum_{l=1}^{M} R_{kl}^{n} V_{kl}^{2} \qquad (1)$$

where R_{kl} is a similarity distance measure between the kth pixel and the centroid of class l, and is defined as follows:

$$R_{kl} = \|X_k - \bar{X}_l\| \qquad (2)$$

Where X_k is the P-features vector, for color images, P=3 in the RGB color space, as intensities of the kth pixel,

and $\overline{X}_l$ is the centroid of class l, and is defined as follows:

$$\overline{X}_l = \frac{\sum_{k=1}^{N} X_k V_{kl}}{n_l} \qquad (3)$$

where n_l is the number of pixels in class l. In case of n=2, the energy in (1), could be considered as the sum of squared errors, V_{kl} is the output of the kl^{th} neuron. UHNNC uses the winner-takes-all learning as the input-output function for the kth row to assign a label m to the pixel and is given by:

$$\begin{cases} V_{kl}(t+1) = 1, & \text{if } U_{kl} = Max\{U_{kl}(t), \forall\, l\} \\ V_{kl}(t+1) = 0; & \text{otherwise} \end{cases} \qquad (4)$$

the minimization is achieved by using UHNNC and by solving a set of motion equations satisfying:

$$\frac{\partial U_i}{\partial t} = -\mu(t)\frac{\partial E}{\partial V_i} \qquad (5)$$

where U_i and V_i are respectively the input and the output of the ith neuron, $\mu(t)$ is as defined in [46] a scalar positive function of time used to increase the convergence speed of the HNN as:

$$\mu(t) = t * (T_s - t) \qquad (6)$$

by applying the relation (5) to equation (1), we get a set of neural dynamics given by:

$$\frac{dU_{kl}}{dt} = -\mu(t)(R_{kl}^n V_{kl}) \qquad (7)$$

The UHNNC segmentation algorithm could be summarized in the following steps:

1. Initialize the input of neurons to random values.

2. Apply the input-output relation given in (4) to obtain the new output value for each neuron, establishing the assignment of pixel to classes.

3. Compute the centroid for each class with respect to the equation (3).

4. Solve the set of differential equation in (5) to update the input of each neuron as:

$$U_{kl}(t+1) = U_{kl}(t) + \frac{dU_{kl}}{dt} \qquad (8)$$

5. Repeat from step 2 until convergence (t = Ts), then terminate.

3. Segmentation Results

Prostate cancer has a slow rate of growth and most tumors remain organ confined for longer than other

malignancies. Because of these features, clinicians have been working to find a reliable way of detecting it early so that potentially life-saving treatments can be implemented promptly [48].

To date, prostate specific antigen (PSA) testing has provided a relatively simple means of population screening for prostate cancer. Unfortunately, however, PSA does not diagnose prostate cancer with certainty as its serum value can be elevated in both benign and malignant conditions of the prostate and not all men with prostate cancer will have high PSA levels. In addition, where prostate cancer is detected early, clinically indolent cancers may be over diagnosed, resulting in overtreatment, and men may experience side effects from untoward treatment that reduce their quality of life. There may also be unnecessary costs and burdens to our health care system. However, as active surveillance is increasingly being adopted as a first-line treatment for men with 'very low' and 'low' risk disease, the risks of overtreatment have been substantially reduced; some studies report up to 40 percent of newly diagnosed men enter this treatment pathway [48-49].

A good review of conventional histological practice in cancer diagnosis can be found in [50], where it is mentioned that few research efforts have been dedicated to the development of quantitative techniques in order to achieve accurate, robust, and reproducible diagnosis and grading in histological images. Diamond et al. [50, 51] used morphometric and texture features to identify stroma, normal, and the remaining tissue is classified into cancerous regions based on a texture feature as shown in Figure 3. [50].
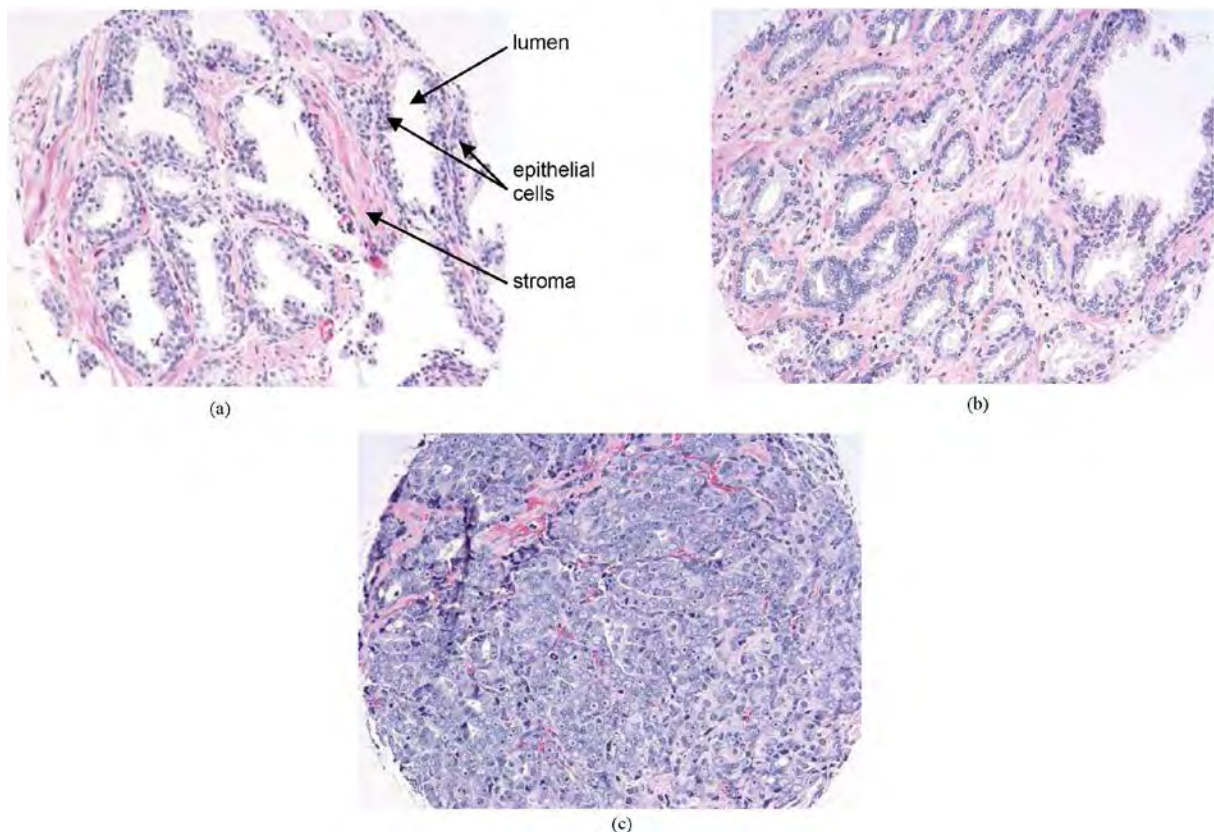

Figure 3: Samples of H&E-stained prostateTMA cores showing varying degrees of differentiation: (a) normal, (b) grade 2 (well-differentiated) cancer, and (c) grade 5 (poorly differentiated) cancer [50].

In this study, we use the population ratio between the different classes of the segmentation result to show the effect of the PSA testing as mentioned earlier with PSMA-1-Pc413 and PSMA-1-IR700. Figure 4.1 represents the control of PC3pip tumor receiving PSMA-1-PC413. Mice received 0.5 mg/kg of PSMA-1-PC413 and tumors were taken out at 48 hours post injection without light irradiation. Figure 4.2 shows the segmentation result of the raw image shown in Figure 4.1 obtained using UHNNC with 4 classes as predefined number of classes. The population ration of class1 and class2 is equal to 0.964, and the same ratio between class3 and class4 is 0.813, the most populated class is taken as a denominator of the ratio. These ration indicates also the similarity between the classes in term of density of their populations. However, these ratios are global, with respect to the image under study, their values will more significant for a Local Region of Interest (ROI) of the scene.
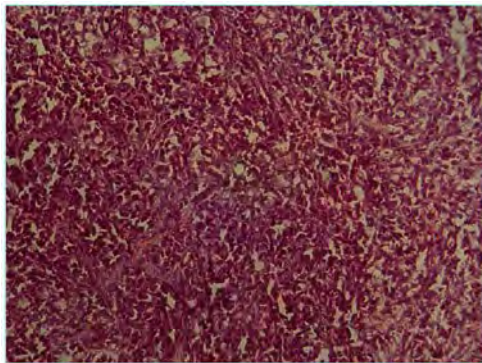
Figure 4.1: Figure2. (A) PC3pip tumor; (0.5 mg/kg PSMA-1-Pc413); (no light irradiation)
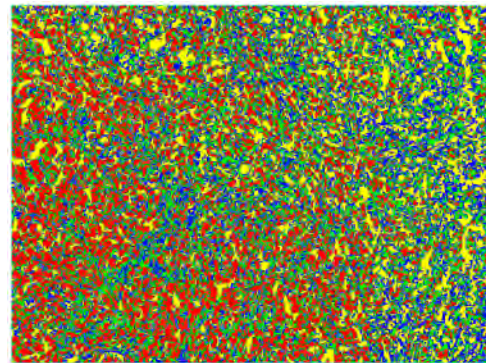
Figure 4.2: Segmentation results of the image in Figure 4.1 using the above described UHNNC. into 4 classes

Classes
- ☑ ⬛ 0: Unclassified
- ☑ 🟥 1: Class 1
- ☑ 🟩 2: Class 2
- ☑ 🟦 3: Class 3
- ☑ 🟨 4: Class 4

Class Distribution Summary
Unclassified: 0 points (0.000%)
Class 1: 216,344 points (28.147%)
Class 2: 224,200 points (29.169%)
Class 3: 180,892 points (23.535%)
Class 4: 147,176 points (19.148%)
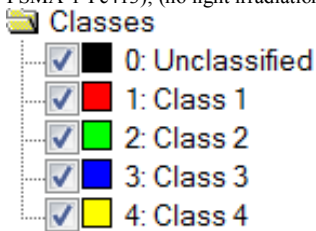
Figure 4.3 Classes Color Keys Table of the segmentation result shown in Figure 4. 2
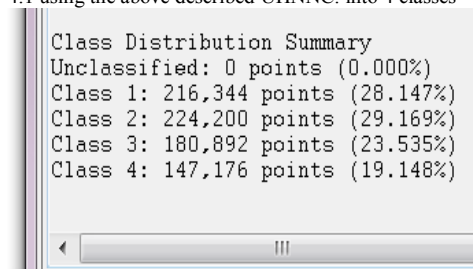
Figure 4.4 Classes Statistics Table of the segmentation result shown in Figure 4. 2
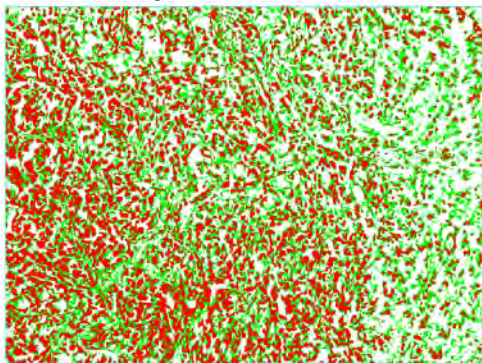

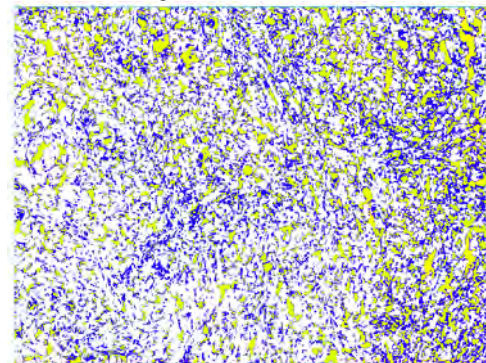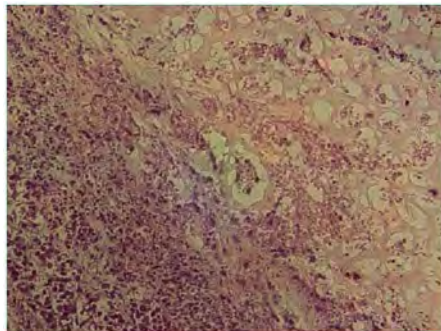Figure 4. 5 Display of Class 1 and Class 2 extracted from the segmentation result shown in Figure 4. 2

Figure 4. 6 Display of Class 3 and Class 4 extracted from the segmentation result shown in Figure 4. 2

Figure 4: Segmentation result of the raw image shown in Figure 2. A. represents PC3pip tumor; (0.5 mg/kg PSMA-1-Pc413); (no light irradiation) obtained using UHNN with 4 classes as predefined number of classes.

Figure 5.1 represents the control of PC3pip tumors receiving PSMA-1-Pc413 and treated with 150J/cm2 light. Mice received 0.5 mg/kg of PSMA-1-PC413, irradiated with 150J/cm2 light at 24 hours post injection. Tumors were taken out at 24 hours post PDT treatment. Figure 4.2 shows the segmentation result of the raw image shown in Figure 5.1 obtained using UHNNC with 4 classes as predefined number of classes. The population ration of class1 and class2 is equal to 0.621, and the same ratio between class3 and class4 is 0.788, the most populated class is taken as a denominator of the ratio. The ration of class1 and class2 indicates a considerable global change in the population of one of the two classes, and a little variation in the population of class3 and class4, as compared to the results shown in Figure 4. The results in Figure 4 and Figure 5 indicate the effect of the theranostic PSMA-1-PDT agent PSMA-1-Pc413 on the prostate cancer cells, which needs more explanation and analysis as cells interaction with the agent.

Figure 5.1: Figure2. (B) PC3pip tumor (0.5 mg/kg PSMA-1-Pc413) with (150J/cm2 light irradiation)
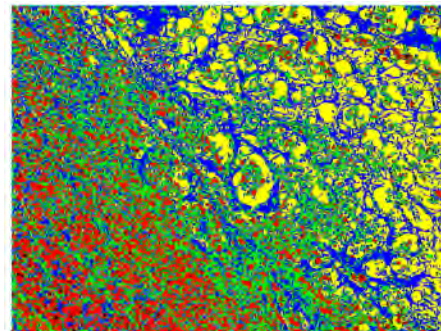

Figure 5.2: Segmentation results of the image in Figure 5.1 using the above described UHNNC. into 4 classes
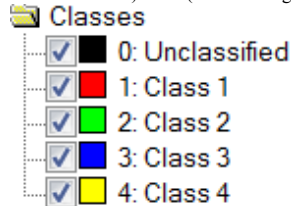

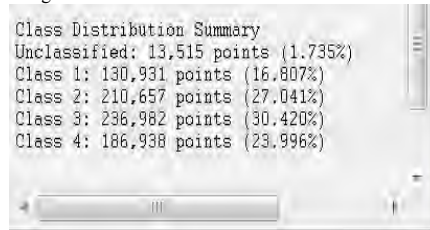Figure 5.3 Classes Color Keys Table of the segmentation result shown in Figure 5. 2

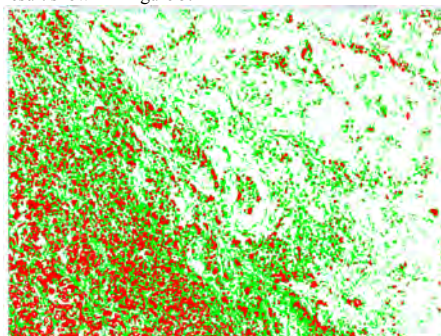Figure 5.4 Classes Statistics Table of the segmentation result shown in Figure 5. 2

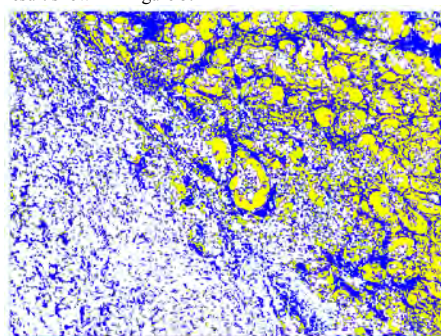Figure 5.5 Display of Class 1 and Class 2 extracted from the segmentation result shown in Figure 5. 2

Figure 5.6 Display of Class 3 and Class 4 extracted from the segmentation result shown in Figure 5.2

Figure 5: Segmentation result of the raw image shown in Figure 2. B. represents PC3pip tumor (0.5 mg/kg PSMA-1-Pc413) with (150J/cm2 light irradiation) obtained using UHNNC with 4 classes as predefined number of cluster.

Figure 6.1 represents the control of PC3pip tumor receiving 0.5 mg/kg PSMA-1-IR700 and tumors were taken out at 48 hours post injection without light irradiation. Figure 6.2 shows the segmentation result of the raw image shown in Figure 6.1 obtained using UHNNC with 4 classes as predefined number of classes. The population ration of class1 and class2 is equal to 0.897, and the same ratio between class3 and class4 is 0.886, the most populated class is taken as a denominator of the ratio. These ration indicates also the similarity between the classes in term of density of their populations.
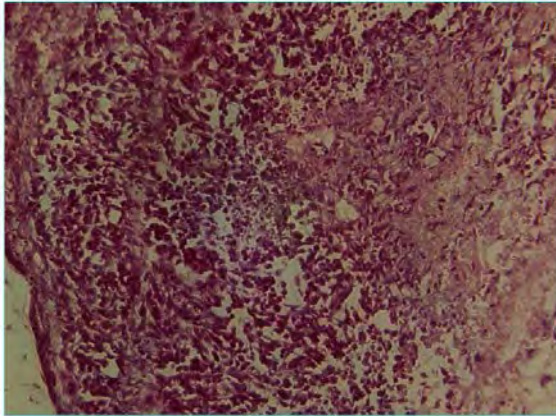

Figure 6.1: Figure2. (C) PC3pip tumor (0.5 mg/kg PSMA-1-IR700) (no light irradiation)
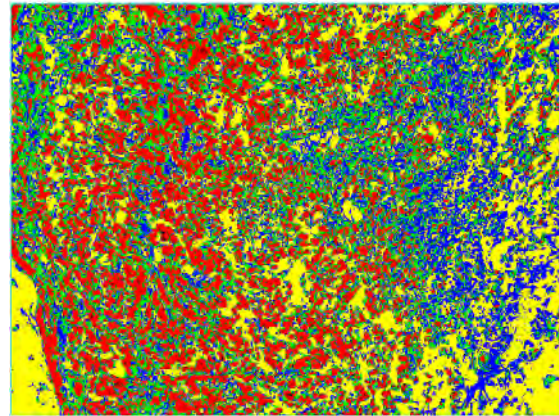

Figure 6.2: Segmentation results of the image in Figure 6.1 using the above described UHNNC. into 4 classes

Figure 6.3 Classes Color Keys Table of the segmentation result shown in Figure 6. 2

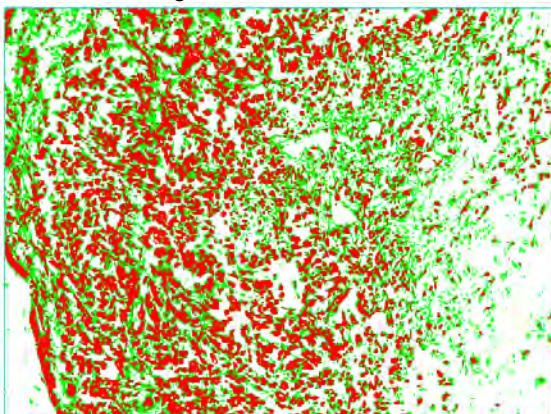Figure 6.4 Classes Statistics Table of the segmentation result shown in Figure 6. 2

Figure 6. 5 Display of Class 1 and Class 2 extracted from the segmentation result shown in Figure 6. 2

Figure 6. 6 Display of Class 3 and Class 4 extracted from the segmentation result shown in Figure 6. 2
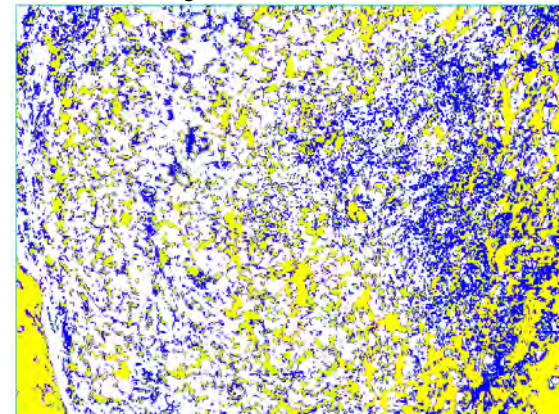
Figure 6: Segmentation result of the raw image shown in Figure 2. (C) PC3pip tumor (0.5 mg/kg PSMA-1-IR700) (no light irradiation) obtained using UHNNC with 4 classes as predefined number of cluster.

Figure 7.1 represents the control of PC3pip tumors receiving 0.5 mg/kg PSMA-1-IR700 and treated with 150J/cm2 light. Mice received 0.5 mg/kg of PSMA-1-IR700, irradiated with 50J/cm2 light at 24 hours post injection. Figure 7.2 shows the segmentation result of the raw image shown in Figure 1.1 obtained using UHNNC with 4 classes as predefined number of classes. The population ratio of class1 and class2 is equal to 0.806, and the same ratio between class3 and class4 is 0.874, the most populated class is taken as a denominator of the ratio. The ratio of class1 and class2 indicates an inconsiderable global change in the population of one of the two classes, and a little variation in the population of class3 and class4, as compared to the ratios shown with Figure 6. The results in Figure 6 and Figure 7 indicate the effect of the theranostic PSMA-1-IR700 agent on the prostate cancer cells, which needs more explanation and analysis as cells interaction with the agent.
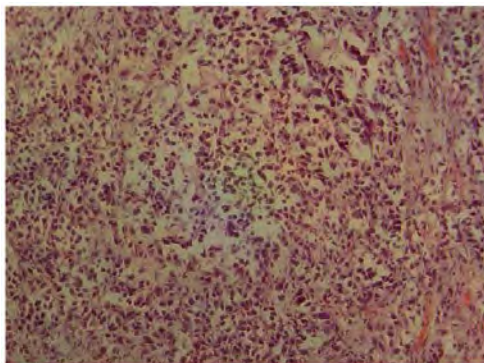

Figure 7.1: Figure2. (D) PC3pip tumor; (0.5 mg/kg PSMA-1-IR700) With (50J/cm2 light irradiation)
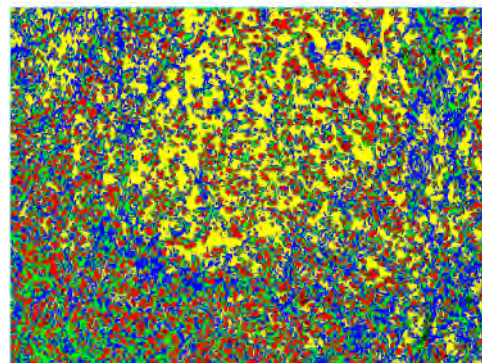

Figure 7.2: Segmentation results of the image in Figure 7.1 using the above described UHNNC. into 4 classes

Figure 7.3 Classes Color Keys Table of the segmentation result shown in Figure 7. 2

Figure 7.4 Classes Statistics Table of the segmentation result shown in Figure 7. 2

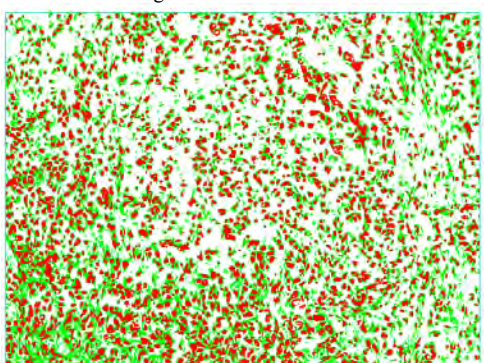Figure 7. 5 Display of Class 1 and Class 2 extracted from the segmentation result shown in Figure 7. 2

Figure 7. 6 Display of Class 3 and Class 4 extracted from the segmentation result shown in Figure 7. 2
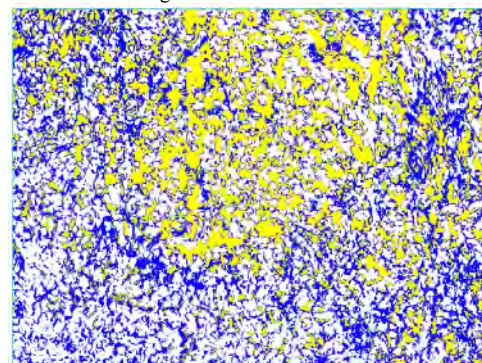
Figure 7: Segmentation result of the raw image shown in Figure. (D) PC3pip tumor (0.5 mg/kg PSMA-1-IR700) with (50J/cm2 light irradiation) obtained using UHNNC with 4 classes as predefined number of cluster.

4. Conclusion

 In this paper we have presented the use of a designed dual-functional PSMA-1-PDT conjugates to serve as anti-cancer agents. The segmentation of the *in vivo* imaging results showed that both PSMA-1-Pc413 and PSMA-1-IR700 can selectively accumulate in PSMA-positive PC3pip tumor. The analysis of these results with more affinity to small ROIs would help to achieve more accurate diagnosis.

Acknowledgments

References

[1]. Hankey BF, Feuer EJ, Clegg LX, et al. Cancer surveillance series: interpreting trends in prostate cancer--part I: Evidence of the effects of screening in recent prostate cancer incidence, mortality, and survival rates. Journal of the National Cancer Institute 1999; 91(12):1017-24.

[2]. Siegel RL, Miller KD, Jemal A. Cancer statistics, 2015. CA Cancer J Clin;65(1):5-29.

[3]. Jermal A, Siegel, R., Ward, E., Murray, T., Xu, J., Smigal, C., et al. Cancer Statistics, 2006. CA Cancer J Clin 2006;56:106.

[4]. Momma T, Hamblin MR, Wu HC, Hasan T. Photodynamic therapy of orthotopic prostate cancer with benzoporphyrin derivative: local control and distant metastasis. Cancer research 1998;58(23):5425-31.

[5]. Swanson GP, Riggs M, Hermans M. Pathologic findings at radical prostatectomy: risk factors for failure and death. Urol Oncol 2007;25(2):110-4.

[6]. Swanson GP, Lerner SP. Positive margins after radical prostatectomy: implications for failure and role of adjuvant treatment. Urol Oncol;31(5):531-41.

[7]. Theiss M, Wirth MP, Manseck A, Frohmuller HG. Prognostic significance of capsular invasion and capsular penetration in patients with clinically localized prostate cancer undergoing radical prostatectomy. Prostate 1995;27(1):13-7.

[8]. Wright JL, Dalkin BL, True LD, et al. Positive surgical margins at radical prostatectomy predict prostate cancer specific mortality. The Journal of Urology 2010;183(6):2213-8.

[9]. Box GN, Ahlering TE. Robotic radical prostatectomy: long-term outcomes. Current Opinion in Urology 2008;18(2):173-9.

[10]. Walsh PC, Lepor H, Eggleston JC. Radical prostatectomy with preservation of sexual function: anatomical and pathological considerations. The Prostate 1983;4(5):473-85.

[11]. Van der Aa F, Joniau S, De Ridder D, Van Poppel H. Potency after unilateral nerve sparing surgery: a report on functional and oncological results of unilateral nerve sparing surgery. Prostate Cancer and Prostatic Diseases 2003;6(1):61-5.

[12]. McClure TD, Margolis DJ, Reiter RE, et al. Use of MR imaging to determine preservation of the neurovascular bundles at robotic-assisted laparoscopic prostatectomy. Radiology 2012;262(3):874-83.

[13]. Burnett AL, Aus G, Canby-Hagino ED, et al. Erectile function outcome reporting after clinically

localized prostate cancer treatment. The Journal of Urology 2007;178(2):597-601.

[14]. Kundu SD, Roehl KA, Eggener SE, Antenor JA, Han M, Catalona WJ. Potency, continence and complications in 3,477 consecutive radical retropubic prostatectomies. The Journal of Urology 2004;172(6 Pt 1):2227-31.

[15]. Penson DF, McLerran D, Feng Z, et al. 5-year urinary and sexual outcomes after radical prostatectomy: results from the prostate cancer outcomes study. The Journal of Urology 2005;173(5):1701-5.

[16]. Saranchuk JW, Kattan MW, Elkin E, Touijer AK, Scardino PT, Eastham JA. Achieving optimal outcomes after radical prostatectomy. Journal of Clinical Oncology : official journal of the American Society of Clinical Oncology 2005;23(18):4146-51.

[17]. Thompson I, Thrasher JB, Aus G, et al. Guideline for the management of clinically localized prostate cancer: 2007 update. The Journal of Urology 2007;177(6):2106-31.

[18]. Neuman BP, Eifler JB, Castanares M, et al. Real-time, near-infrared fluorescence imaging with an optimized dye/light source/camera combination for surgical guidance of prostate cancer. Clin Cancer Res;21(4):771-80.

[19]. Agostinis P, Berg K, Cengel KA, et al. Photodynamic therapy of cancer: an update. CA Cancer J Clin;61(4):250-81.

[20]. Anand S, Ortel BJ, Pereira SP, Hasan T, Maytin EV. Biomodulatory approaches to photodynamic therapy for solid tumors. Cancer Lett;326(1):8-16.

[21]. Dougherty TJ, Gomer CJ, Henderson BW, et al. Photodynamic therapy. J Natl Cancer Inst 1998; 90(12):889-905.

[22]. Lovell JF, Liu TW, Chen J, Zheng G. Activatable photosensitizers for imaging and therapy. Chem Rev;110 (5):2839-57.

[23]. Brown SB, Brown EA, Walker I. The present and future role of photodynamic therapy in cancer treatment. Lancet Oncol 2004;5(8):497-508.

[24]. Juzeniene A, Peng Q, Moan J. Milestones in the development of photodynamic therapy and fluorescence diagnosis. Photochem Photobiol Sci 2007;6(12):1234-45.

[25]. Casas A, Di Venosa G, Hasan T, Al B. Mechanisms of resistance to photodynamic therapy. Curr Med Chem;18(16):2486-515.

[26]. Horoszewicz JS, Kawinski E, Murphy GP. Monoclonal antibodies to a new antigenic marker in epithelial prostatic cells and serum of prostatic cancer patients. Anticancer Res 1987;7(5B):927-35.

[27]. Kawakami M, Okaneya T, Furihata K, Nishizawa O, Katsuyama T. Detection of prostate cancer cells circulating in peripheral blood by reverse transcription-PCR for hKLK2. Cancer Res 1997;57(19):4167-70.

[28]. Wright GL, Jr., Grob BM, Haley C, et al. Upregulation of prostate-specific membrane antigen after androgen-deprivation therapy. Urology 1996;48(2):326-34.

[29]. Ross JS, Sheehan CE, Fisher HA, et al. Correlation of primary tumor prostate-specific membrane antigen expression with disease recurrence in prostate cancer. Clin Cancer Res 2003;9(17):6357-62.

[30]. Mitsiades CS, Lembessis P, Sourla A, Milathianakis C, Tsintavis A, Koutsilieris M. Molecular staging by RT-pCR analysis for PSA and PSMA in peripheral blood and bone marrow samples is an independent predictor of time to biochemical failure following radical prostatectomy for clinically

localized prostate cancer. Clin Exp Metastasis 2004;21(6):495-505.

[31]. Chang SS, O'Keefe DS, Bacich DJ, Reuter VE, Heston WD, Gaudin PB. Prostate-specific membrane antigen is produced in tumor-associated neovasculature. Clin Cancer Res 1999;5(10):2674-81.

[32]. Foss CA, Mease RC, Fan H, et al. Radiolabeled small-molecule ligands for prostate-specific membrane antigen: in vivo imaging in experimental models of prostate cancer. Clin Cancer Res 2005;11(11):4022-8.

[33]. Chen Y, Dhara S, Banerjee SR, et al. A low molecular weight PSMA-based fluorescent imaging agent for cancer. Biochem Biophys Res Commun 2009;390(3):624-9.

[34]. Banerjee SR, Foss CA, Castanares M, et al. Synthesis and evaluation of technetium-99m- and rhenium-labeled inhibitors of the prostate-specific membrane antigen (PSMA). J Med Chem 2008;51(15):4504-17.

[35]. Bander NH, Milowsky MI, Nanus DM, Kostakoglu L, Vallabhajosula S, Goldsmith SJ. Phase I trial of 177lutetium-labeled J591, a monoclonal antibody to prostate-specific membrane antigen, in patients with androgen-independent prostate cancer. J Clin Oncol 2005;23(21):4591-601.

[36]. Wang X, Ma D, Olson WC, Heston WD. In vitro and in vivo responses of advanced prostate tumors to PSMA ADC, an auristatin-conjugated antibody to prostate-specific membrane antigen. Mol Cancer Ther;10(9):1728-39.

[37]. Kuroda K, Liu H, Kim S, Guo M, Navarro V, Bander NH. Saporin toxin-conjugated monoclonal antibody targeting prostate-specific membrane antigen has potent anticancer activity. Prostate;70(12):1286-94.

[38]. Huang SS, Wang X, Zhang Y, Doke A, Difilippo FP, Heston WD. Improving the biodistribution of PSMA-targeting tracers with a highly negatively charged linker. Prostate;74(7):702-13.

[39]. Wang X, Huang SS, Heston WD, Guo H, Wang BC, Basilion JP. Development of targeted near-infrared imaging agents for prostate cancer. Mol Cancer Ther;13(11):2595-606.

[40]. Miller JD, Baron ED, Scull H, et al. Photodynamic therapy with the phthalocyanine photosensitizer Pc 4: the case experience with preclinical mechanistic and early clinical-translational studies. Toxicol Appl Pharmacol 2007; 224(3):290-9.

[41]. Mitsunaga M, Ogawa M, Kosaka N, Rosenblum LT, Choyke PL, Kobayashi H. Cancer cell-selective in vivo near infrared photoimmunotherapy targeting specific membrane molecules. Nat Med;17(12):1685-91.

[42]. Nakajima T, Sano K, Choyke PL, Kobayashi H. Improving the efficacy of Photoimmunotherapy (PIT) using a cocktail of antibody conjugates in a multiple antigen tumor model. Theranostics;3(6):357-65.

[43]. Watanabe R, Hanaoka H, Sato K, et al. Photoimmunotherapy targeting prostate-specific membrane antigen: are antibody fragments as effective as antibodies? J Nucl Med;56(1):140-4.

[44]. Taatjes DJ, Sobel BE, Budd RC. Morphological and cytochemical determination of cell death by apoptosis. Histochem Cell Biol 2008;129(1):33-43.

[45]. Zhen Ma1, João Manuel R. S. Tavares2 and Renato Natal Jorge2. Segmentation of Structures in Medical Images: Review and a New Computational Framework, Proceedings of the Intl. Symposium CMBBE2008.

[46]. Rachid Sammouda, Mohammed Sammouda, and Jamel Abu Hassan "CT Images Analysis for Early

Detection of Lung Cancer", International Journal of Innovative Computing, Information and Control (IJICIC), Vol. 4, No. 11, Nov. 2008.

[47]. Rachid Sammouda, Nuru Adgaba, Ameur Touir and Ahmed Al-Ghamdi, "Agriculture Satellite Image Segmentation using a Modified Artificial Hopfield Neural Network", Journal of Computers in Human, Vol. 30, pp.436–441, 2014.

[48]. Hugosson J, Carlsson S, Aus G, et al. 2010. Mortality results from the Göteborg randomized population based prostate cancer screening trial. Lancet Oncology 11(8): 725–32.

[49]. New Zealand, Ministry of Health, Citation: Prostate Cancer Taskforce. 2012. Diagnosis and Management of Prostate Cancer in New Zealand Men: Recommendations from the Prostate Cancer Taskforce. Wellington: Ministry of Health; Published in May 2013 by the Ministry of Health PO Box 5013, Wellington 6145, New Zealand ISBN 978-0-478-40264-3 (online) HP 5647. This document is available at www.health.govt.nz.

[50]. Ali Tabesh*, Member, IEEE, Mikhail Teverovskiy, Ho-Yuen Pang, Vinay P. Kumar, David Verbel, Angeliki Kotsianti, and Olivier Saidi, "Multifeature Prostate Cancer Diagnosis and Gleason Grading of Histological Images", IEEE TRANSACTIONS ON MEDICAL IMAGING, VOL. 26, NO. 10, OCTOBER 2007.

[51]. J. Diamond, N. Anderson, P. Bartels, R. Montironi, and P. Hamilton, "The use of morphological characteristics and texture analysis in the identification of tissue composition in prostatic neoplasia," Human Pathology, vol. 35, pp. 1121–1131, 2004.